PHYSICAL REVIEW C **106**, 035201 (2022)

Differential cross sections and photon beam asymmetries of η photoproduction on the proton at $E_\gamma = 1.3$–2.4 GeV

T. Hashimoto,[1,2] T. Nam,[1] N. Muramatsu,[3] J. K. Ahn,[4] W. C. Chang,[5] J. Y. Chen,[6] M. L. Chu,[5] S. Daté,[7,1] T. Gogami,[2]
H. Goto,[1] H. Hamano,[1] Q. H. He,[8] K. Hicks,[9] T. Hiraiwa,[10] Y. Honda,[3] T. Hotta,[1] H. Ikuno,[1] Y. Inoue,[3] T. Ishikawa,[3]
I. Jaegle,[11] J. M. Jo,[4] Y. Kasamatsu,[1] H. Katsuragawa,[1] S. Kido,[3] Y. Kon,[1] S. Masumoto,[12] Y. Matsumura,[3] M. Miyabe,[3]
K. Mizutani,[11] T. Nakamura,[13] T. Nakano,[1] M. Niiyama,[14] Y. Nozawa,[15] Y. Ohashi,[7,1] H. Ohnishi,[3] T. Ohta,[15] K. Ozawa,[16]
C. Rangacharyulu,[17] S. Y. Ryu,[1] Y. Sada,[3] T. Shibukawa,[12] H. Shimizu,[3,1] R. Shirai,[3] K. Shiraishi,[3] E. A. Strokovsky,[18,1]
Y. Sugaya,[1] M. Sumihama,[13,1] S. Suzuki,[7] S. Tanaka,[1] Y. Taniguchi,[3] A. Tokiyasu,[3] N. Tomida,[1] Y. Tsuchikawa,[19] T. Ueda,[3]
H. Yamazaki,[20] R. Yamazaki,[3] Y. Yanai,[1] T. Yorita,[1] C. Yoshida,[3] and M. Yosoi[1]
(LEPS2/BGOegg Collaboration)

[1] *Research Center for Nuclear Physics, Osaka University, Ibaraki, Osaka 567-0047, Japan*
[2] *Department of Physics, Kyoto University, Kyoto 606-8502, Japan*
[3] *Research Center for Electron Photon Science, Tohoku University, Sendai, Miyagi 982-0826, Japan*
[4] *Department of Physics, Korea University, Seoul 02841, Republic of Korea*
[5] *Institute of Physics, Academia Sinica, Taipei 11529, Taiwan*
[6] *National Synchrotron Radiation Research Center, Hsinchu 30076, Taiwan*
[7] *Japan Synchrotron Radiation Research Institute (SPring-8), Sayo, Hyogo 679-5198, Japan*
[8] *Department of Nuclear Science & Engineering, College of Material Science and Technology, Nanjing University of Aeronautics and Astronautics, Nanjing 210016, China*
[9] *Department of Physics and Astronomy, Ohio University, Athens, Ohio 45701, USA*
[10] *RIKEN SPring-8 Center, Sayo, Hyogo 679-5148, Japan*
[11] *Thomas Jefferson National Accelerator Facility, Newport News, Virginia 23606, USA*
[12] *Department of Physics, University of Tokyo, Tokyo 113-0033, Japan*
[13] *Department of Education, Gifu University, Gifu 501-1193, Japan*
[14] *Department of Physics, Kyoto Sangyo University, Kyoto 603-8555, Japan*
[15] *Department of Radiology, The University of Tokyo Hospital, Tokyo 113-8655, Japan*
[16] *Institute of Particle and Nuclear Studies, High Energy Accelerator Research Organization (KEK), Tsukuba, Ibaraki 305-0801, Japan*
[17] *Department of Physics and Engineering Physics, University of Saskatchewan, Saskatoon, Saskatchewan S7N 5E2, Canada*
[18] *Laboratory of High Energy Physics, Joint Institute for Nuclear Research, Dubna, Moscow Region 142281, Russia*
[19] *J-PARC Center, Japan Atomic Energy Agency, Tokai, Ibaraki 319-1195, Japan*
[20] *Radiation Science Center, High Energy Accelerator Research Organization (KEK), Tokai, Ibaraki 319-1195, Japan*

(Received 28 February 2022; revised 8 July 2022; accepted 2 August 2022; published 15 September 2022)

We report exclusive measurements for the η photoproduction on a proton target. The differential cross sections and photon beam asymmetries of the $\gamma p \rightarrow \eta p$ reaction are measured in a center-of-mass energy (W) range of 1.82–2.32 GeV and a polar angle range of $-1.0 < \cos\theta^{\eta}_{\mathrm{c.m.}} < 0.6$ by using a large acceptance calorimeter (BGOegg) and forward-angle charged-particle detectors at the SPring-8 LEPS2 beamline. The reaction is identified with a kinematic fitting method to select a recoil proton and two photons produced in an η meson decay. A bump structure at $W = 2.0$–2.3 GeV in the differential cross section is confirmed at extremely backward η polar angles, where the existing data are inconsistent with each other. This bump structure is likely associated with high-spin resonances that couple with $s\bar{s}$ quarks. The photon beam asymmetries in a wide η polar angle range for the photon beam energies above 2.1 GeV are reported for the first time, providing an additional constraint to nucleon resonance studies at high energies.

DOI: 10.1103/PhysRevC.106.035201

I. INTRODUCTION

The experimental data of meson photoproduction and pion-nucleon (πN) scattering in conjunction with partial wave analyses (PWAs) are major sources of the information on baryon resonances for 1–3 GeV center-of-mass energies. The Particle Data Group summarizes the latest lists of the resonances in Tables 80.1 and 80.2 of Ref. [1]. The constituent quark models are moderately successful in reproducing the mass spectrum, especially in the energy range below 1.8 GeV [2]. However, the predicted resonance masses are often not consistent with experimental results. For instance, the well-established Roper resonance $N(1440)1/2^+$ is calculated to lie above the lowest s-wave resonance $N(1535)1/2^-$ in the quark models [3]. In addition, it is known that many predicted states are missing from experimental searches in the range above $W = 1.8$ GeV. Because the mass spectra are sensitive to the hadron structure beyond the existing constituent quark models, it is necessary to clarify the spectral information from the experimental side for better understanding of QCD.

Meson photoproduction has advantages in the investigation of excited baryons thanks to many possibilities of final-state meson-baryon combinations. It can be sensitive to the states whose coupling to the πN scattering is weak. The spin information of intermediate resonances can also be obtained by utilizing the high polarization of a photon beam. Photoproduction experiments are thus getting more popular in modern baryon studies. Here the photoproduction of an η meson is a prime example of such research subjects. The η meson photoproduction has a reasonably large cross section, and it offers an attractive capability of coupling with the $s\bar{s}$ component in an s-channel baryon resonance. Moreover, the η meson is an isoscalar particle and can only couple to isospin $1/2$ resonances. The η photoproduction works as an isospin filter for the complex spectra of baryon resonances.

Several experimental results of the η photoproduction on the proton around the center-of-mass energies (W) of 2 GeV have been published in the last two decades. Differential cross sections at backward polar angles were measured by the LEPS Collaboration [4], while those in wide angular regions were reported by the CLAS [5], CBELSA/TAPS [6], and MAMI A2 [7] Collaborations. The CLAS and CBELSA/TAPS experiments also showed the results of the photon beam asymmetries in Refs. [8,9]. In the differential cross sections measured by the LEPS, CLAS, and CBELSA/TAPS experiments, a bump structure was seen at $W > 2$ GeV for the kinematical region of backward η angles. However, the shapes and strengths of the bump structure in these differential cross sections are significantly inconsistent with each other, causing a controversial situation. A possible reason for the observed inconsistency may be the existence of unknown systematic uncertainties due to the detector acceptance limitations in those experiments, as discussed later. In addition, there is a case that statistical precision of data is not sufficient for detailed discussions of the consistency. A new measurement that solves these problems is desired for the clarification of the bump structure.

This article reports experimental results for the differential cross sections and photon beam asymmetries of the η photoproduction measured by the SPring-8 LEPS2/BGOegg experiment. The measurement in a wide polar angle region $-1 < \cos\theta^{\eta}_{\mathrm{c.m.}} < 0.6$ is made possible with a large acceptance calorimeter having good resolutions. All the final state products, a proton and an η meson decaying into two γ's, are detected so that the nature of the bump structure can be examined with the clear identification of the exclusive reaction. At the most backward η angles, high-statistics data are available to achieve more reliable studies that have never been done by the previous experiments. The beam asymmetry data for the total energies above 2.1 GeV can also be obtained for the first time with photon-beam linear polarization higher than 90%. Such new data provide valuable information for partial wave analyses including the bump study.

This paper is organized as follows. Section II describes the experimental setup. Data-analysis procedures are provided in Sec. III. In Sec. IV, methods to obtain the differential cross sections and photon beam asymmetries are presented in detail. Experimental results are shown in Sec. V. The obtained results are discussed and compared with several PWA calculations in Sec. VI. Section VII is the summary of the present measurement and results.

II. EXPERIMENTAL SETUP

An experiment to study the η photoproduction was carried out using the LEPS2 beamline at SPring-8. Details of the LEPS2 beamline are described in Ref. [10]. Figure 1 shows the schematic view of detectors in this experiment (the BGOegg experiment). A high-energy photon beam was produced by the backward Compton scattering of 355 nm wavelength ultraviolet laser light from an 8-GeV electron in the storage ring [11]. Four laser beams can be injected simultaneously from the oscillators whose maximum output power is either 16 or 24 W. The maximum energy of the scattered photon is 2.39 GeV at the Compton edge.

The energy of a backwardly scattered photon is measured by the tagging detector system (tagger), the details of which are to be found in Ref. [11]. The tagger consists of two layers of 1-mm-wide scintillating fiber bundles and two layers of 8-mm-wide plastic scintillators to reconstruct the track of a recoil electron from the Compton scattering. A momentum of the recoil electron is determined from its hit position on the tagger, which is located downstream of a storage-ring bending magnet. The photon energy is then calculated event by event using the four-momentum conservation law. A tagger logic signal is formed when coincident hits exist in 8-mm-wide plastic scintillators paired at two layers. This logic signal is used to make a trigger for data acquisition by requiring it with simultaneous hits in at least two crystals of the BGOegg calorimeter, which is the main detector in the present experiment. The hit rate of the tagger logic signal is counted by a scaler to monitor the photon beam flux. The tagger hit rate was in the range of 1–1.8 $\times 10^6$ photon/s during the data collection.

A cylindrical target cell, made of thin polyimide films, is placed in the center of the BGOegg calorimeter. A refrigerator that is connected to a hydrogen gas tank liquefies a part of the sealed gas, and fills the target cell with liquid hydrogen. The measured thickness of the target cell was 54 mm, and the center of the target was shifted 3 mm upstream from the designed center position due to an expansion effect of the target cell. This small shift affects the polar angle measurement of final reaction products and is taken into account in the offline analysis.

The BGOegg calorimeter consists of 1320 bismuth germanate (BGO) crystals with 20 radiation lengths, covering polar angles from 24° to 144°. The crystals are distributed

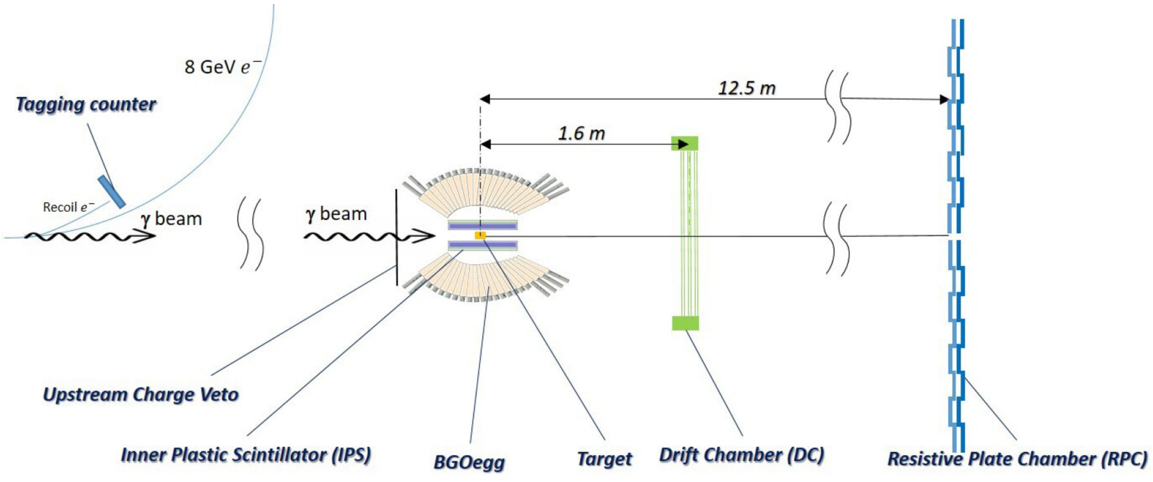

FIG. 1. A schematic drawing of experimental setup at the LEPS2 beamline (top view).

into 22 layers in the polar angle direction with a ring of 60 crystals each. No frame material is inserted between the crystals. The energy calibration for each crystal has been done by iteration so that a distribution for the invariant mass of two γ's, one of which deposits the largest fraction of its energy to the calibrated crystal, should have a peak at the nominal π^0 mass [1]. The energy resolution of the BGOegg calorimeter was evaluated to be 1.4% at the incident γ energy of 1 GeV [12]. The invariant mass resolution of the π^0 is 6.7 MeV/c^2 with a 20-mm-thick carbon target. These resolutions are the world's best among the experiments conducted in a similar energy range. For a BGOegg calorimeter hit, the identification of a charged or neutral particle was performed using the inner plastic scintillator (IPS). The IPS consists of 30 scintillator slabs which are 453 mm long and 5 mm thick. These slabs are arranged in a cylindrical shape around the target.

Charged particles that were emitted to the forward open hole of the BGOegg calorimeter were detected using the drift chamber (DC). The DC consists of six separated planes. Each plane has 80 sense wires with a wire interval of 16 mm. These six planes are divided into three groups by the directions of sense wires, which are tilted at an azimuthal angle of 60° relative to the other groups. The positions of sense wires in a certain plane are shifted by 8 mm relative to those in the other plane belonging to the same group. The position resolution of a DC hit on each plane is about 300 μm. The DC is located 1.6 m downstream of the target, covering polar angles less than 21°.

A time-of-flight (ToF) wall of 32 resistive plate chambers (RPCs), each of which is 250 mm wide and 1000 mm long [13,14], was placed at a distance of 12.5 m from the target to measure the momentum of protons emitted to extremely forward angles. There are eight readout strips along the vertical direction in a chamber, and hit signals are read at both top and bottom ends. Figure 2 shows the size of the ToF wall and the arrangement of RPCs. The time resolution of the RPC is 60–90 ps, providing a good momentum resolution of less than 1% for an incident proton of 2 GeV/c. The RPCs cover the laboratory polar angles less than 6.8° degrees, which correspond to the most backward η polar angles in the center-of-mass frame of the reaction, $\cos\theta^{\eta}_{\mathrm{c.m.}} < -0.95$. The RPC allows the measurement of the differential cross sections of η photoproduction at the most backward angles with full kinematic information, which makes the present analysis more reliable. This extreme angular region is either inaccessible or associated with large uncertainties in other experiments.

A scintillating counter with an effective area of 620 × 620 mm^2 and a thickness of 3 mm was installed just upstream of the BGOegg calorimeter. It was used to veto the e^+e^- pairs contaminating the photon beam.

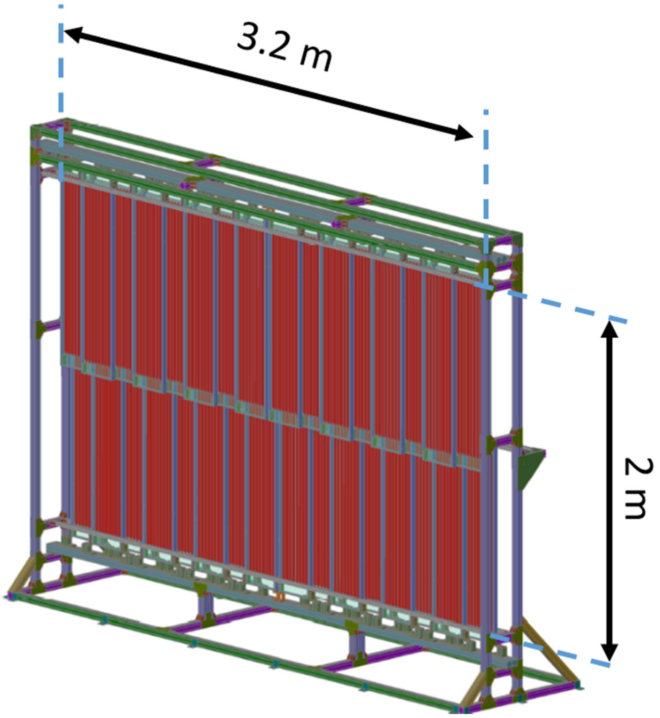

FIG. 2. A three-dimensional figure of ToF wall that is formed by 32 RPCs.

III. DATA ANALYSIS

A. Event reconstruction

A photon produced by Compton scattering is identified offline if a recoil electron track is successfully reconstructed with strict geometrical conditions at the tagger. At first, the recoil electron must hit one or two layers of the scintillating fibers and two layers of the plastic scintillators, following one of the hit patterns that are pre-defined as possible geometrical arrangement for a straight track. Secondly, tight cuts are applied for the timing difference between plastic scintillators and scintillating fibers. The plastic scintillator hit timings are finally averaged to obtain a detection time of the reconstructed track. Its time resolution is 170 ps, which is good enough compared with the interval of electron beam bunches in the storage ring (a multiple of 2 ns). For the unambiguous determination of photon beam energies, offline events pass when only one tagger track is reconstructed at the timing of BGOegg calorimeter hits.

For the measurement of differential cross sections, the tagger reconstruction efficiency was evaluated to compensate for the signal loss due to track reconstruction failure in the offline analysis, multitrack detection in the tagger, and inefficiencies of tagger fibers. The reconstruction efficiency varies from 0.86 to 0.93 depending on the photon beam energy. The typical uncertainty of this reconstruction efficiency is 0.7%. The electromagnetic shower contamination rate due to high momentum recoil electrons hitting the walls of vacuum chambers upstream of the tagger was estimated to be 0.0424 ± 0.0006 [15] at the tagger trigger level. This contamination was sufficiently removed offline by the tight geometrical conditions in the tagger reconstruction.

The photon beam energy of each event was obtained by using a fourth-order polynomial function depending on the tagger hit position. This function was predetermined from a fit to a set of independently measured energies for individual tagger fiber channels. Here, the independent measurement of photon beam energies was done by a kinematic fit to a sample of the reaction $\gamma p \to \pi^0\pi^0 p$ with the information of the final state particles but without that of the tagger. In the kinematic fit, a resolution of the photon beam energy measured by the tagger was simultaneously estimated to be 12.1 MeV. This resolution is predominantly influenced by the electron beam emittance.

The measurement of differential cross sections needs an accurate determination of the photon beam flux. The photon beam flux was derived from a rate of the tagger logic signals, but such counting was influenced by dead time due to a finite signal width of 20 ns. The dead time depends on the tagger trigger rate and the electron filling pattern at SPring-8 [16]. It was typically evaluated to be 10% by a purely stochastic simulation. The integrated counts of tagger logic signals used for the present analysis reach of 3.593×10^{12} after correcting for the dead time.

A part of the photon beam is lost due primarily to pair creations at materials in the long beamline from the Compton scattering point to the target. A transmission rate of the photon beam was estimated to be 0.772 by taking into account the amount of materials. The uncertainty of this value originating from the accuracy of the material thickness was negligibly small. The transmission rate was further corrected by multiplying an additional factor F_{trans}, which was a second-order polynomial function of the photon beam energy (Eq. (1) of Ref. [15]). This correction was necessary because of unexpected beam loss that happened by the cutoff of a peripheral region at a collimator in the experimental periods when the focal length of injected laser light was adjusted to be longer than the designed distance. At lower energies, the Compton scattering produces photons with wider cone angles, and therefore the amount of correction becomes larger. The F_{trans} was obtained in an independent sample by taking the energy-dependent ratio of inclusive π^0 yields to tagger photon counts and normalizing it by the ratio in the period with a good laser focal length. The obtained factor was finally renormalized to one at the highest energy region, where no beam loss was observed.

Two γ's from an η photoproduction reaction are detected using the BGOegg calorimeter. The Moliere radius for BGO is 22.3 mm, which is a little larger than the front size of individual BGO crystals. Therefore, an electromagnetic shower of a γ leaves its energy in multiple crystals around a core where the γ is incident. The crystals with energy deposits are grouped into a "cluster." This cluster consists of several main crystals whose energies are greater than the discriminator threshold at about 10 MeV and neighboring peripheral crystals with smaller energies. The cluster energy was a sum of all the cluster members. A crystal with the largest energy was adopted as the core of a cluster. A cluster timing was determined by using the core crystal. The center of a cluster was evaluated from the energy-weighted average of hit crystal positions. The charge of a cluster was identified by examining an IPS hit on the line between the target and the BGOegg cluster center. Thus, a proton from the η photoproduction is also detectable as a charged particle at the BGOegg calorimeter. The detection efficiency of a proton at the IPS was estimated to be 0.9863 ± 0.0009.

The DC measures only the direction of a charged particle under no magnetic field. A straight line was fitted to each track candidate, which contains five or more layer hits. The fit was performed by taking into account drift distances from individual hit wires and using an additional constraint by the target position. Tracks with the χ^2 probability greater than 1% were accepted for further analysis The efficiency of finding a DC track, including both detection and reconstruction efficiencies, was estimated to be 0.9824 ± 0.0044 by analyzing photoproduction reactions with a forward proton independently detected using the RPC.

A proton hit at the RPC was searched for around the position that was on the extension line of the reconstructed DC track. The hit positions in the horizontal (x) and vertical (y) directions were obtained from the channel number of the hitting strip and the timing difference of hit signals read out at the top and bottom ends of a strip, respectively. The position resolutions in the two directions were $\sigma_x = 7.5$ mm and $\sigma_y = 16$ mm. The reconstruction efficiency of an RPC hit was 0.931 ± 0.023. The velocity of a charged particle was measured from the ToF, and the corresponding momentum was determined by assuming the proton mass for the detected

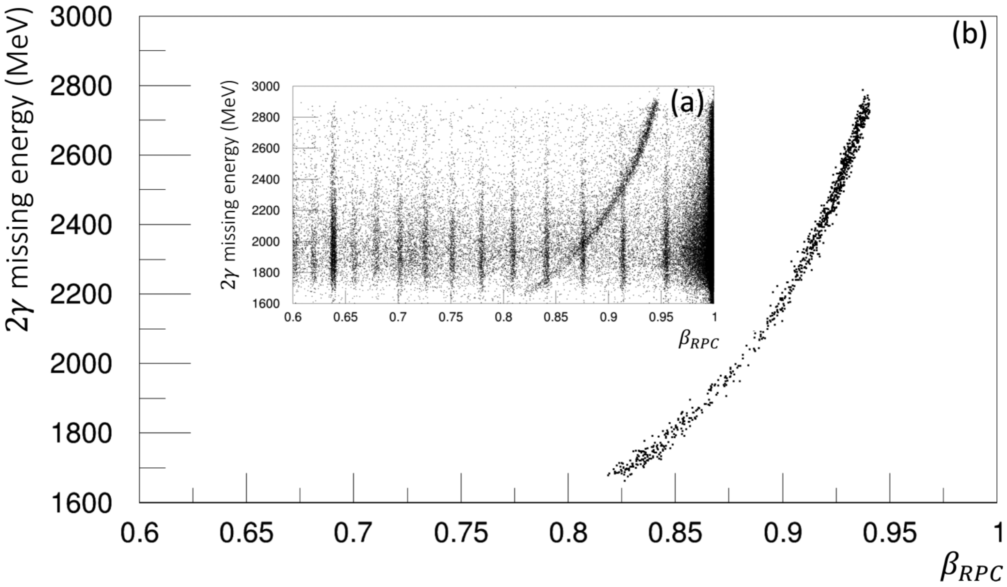

FIG. 3. The correlation between the missing energy of a $\gamma\gamma$ pair detected at the BGOegg calorimeter and the velocity of a charged particle measured using the RPC. The black dots in panel (a) show the data before the kinematic fit but after requiring the existence of two neutral clusters at the BGOegg calorimeter with a loose cut on the missing mass. The vertical bands come from electron events, which originate from the different electron bunches in the SPring-8 storage ring. Panel (b) shows the data after passing the 99% confidence level cut in the kinematic fit.

particle. Protons are well separated from charged pions and electrons by the velocity information if it is combined with the measurement of a meson at the BGOegg calorimeter. Figure 3 shows the correlation between the missing energy of a $\gamma\gamma$ pair detected using the BGOegg calorimeter and the velocity of a charged particle measured using the RPC. While events at the reconstruction level are shown by black dots in the panel (a), only the proton band remains in the panel (b) after the kinematic fit selection of $\gamma p \to \eta p \to \gamma\gamma p$ events with the use of both the RPC and the BGOegg calorimeter.

B. Event selection

In the present analysis, the $\gamma p \to \eta p$ events were extracted from the data collected with the liquid hydrogen target by identifying the η meson in the decay mode into $\gamma\gamma$, whose branching fraction is 0.3941 ± 0.0020 [1]. Event selection conditions are basically the same as those in the published article on π^0 photoproduction [15].

A signal candidate was selected if two neutral clusters were detected at the BGOegg calorimeter and their timings were within ±3 ns of the reference time determined based on the electron bunch where Compton scattering happened. Neutral clusters whose central crystal was found at the most forward or backward edge layer of the BGOegg calorimeter were unused because the correct cluster energy was not able to be measured due to shower leakage. The minimum energy of each cluster was required to be 50 MeV in order to remove accidental hits.

In addition to the neutral clusters, a charged particle was detected as a proton candidate in the wider acceptance defined by a combination of the BGOegg calorimeter, the DC, and the RPC depending on the emission angle. The angular range of $24^\circ < \theta^p_{\text{lab}} < 144^\circ$ $(-0.5 < \cos\theta^\eta_{\text{c.m.}} < 0.6)$ was covered by the BGOegg calorimeter, where the emitted direction was measured based on a line from the target center to the charged cluster core. The timing and minimum energy conditions of charged clusters were the same as those of neutral clusters. Unlike the neutral cluster, the charged clusters whose core was found at the edge layers of the BGOegg calorimeter were used because only the emission angle was measured. Charged particles emitted at the angles $\theta^p_{\text{lab}} < 21^\circ$ $(\cos\theta^\eta_{\text{c.m.}} < -0.5)$ were measured using the DC. In the case of extremely forward emission angles $\theta^p_{\text{lab}} < 6.8^\circ$ $(\cos\theta^\eta_{\text{c.m.}} < -0.95)$, it was possible to perform an additional analysis with the events in which a charged particle was detected at both the DC and the RPC, as described later. The total number of charged particles in a reconstructed event was limited to 1.

After measuring all the final state particles, a kinematic fit was performed by assuming the reaction $\gamma p \to \eta p \to \gamma\gamma p$. Five constraints were defined by a series of equations describing the four-momentum conservation between the initial and final states of the reaction and the equivalence of the $\gamma\gamma$ invariant mass to the nominal η mass. In the equations of four-momentum conservation, the nominal mass of a proton was used for the charged particle. The measured energy and polar and azimuthal angles were varied within the uncertainties determined by detector resolutions. The reaction vertex position along the photon beam direction was also floated with the constraint of the target size. The uncertainties of input variables in the kinematic fit were estimated by using the GEANT4 [17] based simulation package in which the detector setup was realistically implemented with the resolutions to compare the measured values with the true ones. Finally, a 99% confidence level cut was applied to the χ^2 probability of the

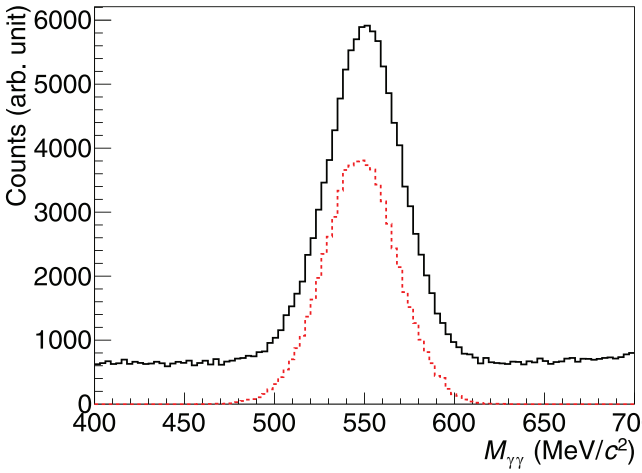

FIG. 4. The invariant mass distributions for $\gamma\gamma$ pairs detected at the BGOegg calorimeter. The black solid histogram shows the events surviving after applying a loose condition, where the missing mass of a $\gamma\gamma$ pair is less than 1200 MeV/c^2. The red dashed histogram shows the events that survive after applying the 99% confidence level cut.

kinematic fit. Figure 4 shows the invariant mass distributions for $\gamma\gamma$ pairs detected at the BGOegg calorimeter. Most of the background was successfully removed without acceptance loss by the confidence level cut. However, the background rejection was incomplete because the proton momentum was not measured in the case only the BGOegg calorimeter or the DC was used for the detection of a charged particle. The background contamination is discussed in the next subsection.

C. Yield extraction with background subtraction

In order to extract signal yields, it is necessary to estimate background contributions in the event sample that remains after the selection described in the previous subsection. After the confidence level cut, kinematical distributions of signals and backgrounds become too similar to be distinguished from each other. Therefore, the amounts of individual background processes were separately estimated by performing a template fitting for the background-enhanced sample with a loose event selection, where cuts were placed on the invariant and missing masses of a $\gamma\gamma$ pair to select an η meson and a proton, respectively. Angular consistency between the detected proton and the missing momentum of a $\gamma\gamma$ pair was also required.

Three background reactions were taken into account in the template fitting: $\gamma p \to \pi^0\pi^0 p$, $\gamma p \to \pi^0\eta p$, and $\gamma p \to \omega p$, in which the mesons decayed into multiple γ's and only two γ's were detected at the BGOegg calorimeter. At first, the signal and above mentioned background processes were generated in Monte Carlo (MC) simulations, and template spectra of the invariant and missing mass distributions for $\gamma\gamma$ pairs were prepared using loose event selection criteria. Characteristic shapes for individual background processes appear in the sideband regions of the plotted distributions. Finally, all of the template histograms were simultaneously fitted to the corresponding invariant and missing mass distributions in the real data at individual kinematic bins, separated in W, $\cos\theta^{\eta}_{\mathrm{c.m.}}$, and azimuthal angles. The entire events were divided into five segments per energy, four segments per polar angle, and eight segments per azimuthal angle.

Figure 5 shows an example of the template fit in a certain kinematic bin. From the template fitting result, the normalization factors of simulated background samples to the real data size were determined. The contamination rate of each background after the confidence level cut of the kinematic fit was then evaluated by applying this cut to individual simulated background samples and taking into account the obtained normalization factors. The signal yields in individual kinematic bins were obtained by subtracting the estimated amount of backgrounds.

To check the validity of this template fitting, the systematic variations of signal yields were evaluated using two additional fitting methods. One was to exclude the ω meson contribution from the fitting to reduce the number of free parameters. For this purpose, a tight invariant mass cut was further applied to suppress the ω contamination. The yield difference from the original template fitting was less than 2% in any kinematic region. The other was to perform the template fitting using only the invariant mass distribution to avoid a possible bias in the signal extraction due to the simultaneous fit to the missing mass distribution. The relative ratios of the three backgrounds were fixed based on the original template fitting, and the total amount of background was treated as a free parameter in this method. The yield difference from the original estimation was less than 6% in all kinematic regions.

The number of events that survived after the kinematic fit was 6.2×10^4 events in the present data. The background ratio was 3.1–36.9% depending on the kinematic bins. This ratio tends to rise as the total energy increases. After the background subtraction, the number of signal yields was estimated to be 5.5×10^4 events. In the final event sample, the background contribution from the target container was evaluated to be negligible by analyzing the data collected with an empty target, where the target cell was filled with vaporized hydrogen gas.

D. Geometrical acceptance

The geometrical acceptance was obtained by the GEANT4-based Monte Carlo (MC) simulation package developed for this experiment. The $\gamma p \to \eta p$ events were generated with an isotropic angular distribution. The same event selection conditions as those in the real data analysis were applied to the generated sample for the evaluation of geometrical acceptance. The cross sections obtained from this acceptance were then fed back to the MC simulation so as to reflect the realistic kinematic distributions in a new round of acceptance calculation. This iterative process ended when a change of the differential cross section from the previous step became smaller than 1%. The typical acceptance is 50% at backward η angles and reduced at forward angles. There is detection sensitivity up to $\cos\theta^{\eta}_{\mathrm{c.m.}} \approx 0.6$.

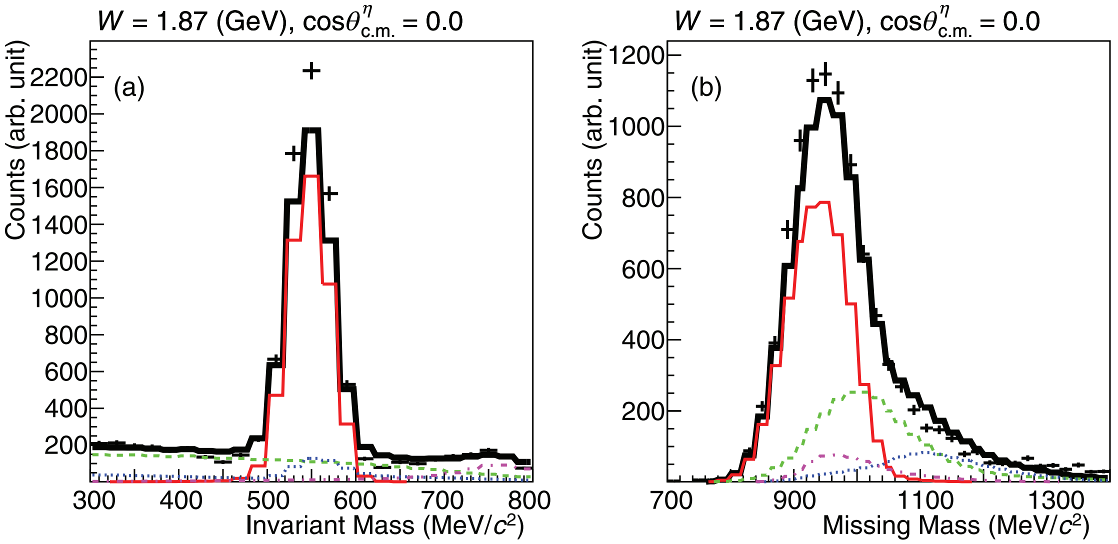

FIG. 5. An example of the template fitting at the kinematic bin of $W = 1.87$ GeV and $\cos\theta^{\eta}_{\mathrm{c.m.}} = 0$. The invariant mass spectrum for $\gamma\gamma$ pairs detected at the BGOegg calorimeter in the real data is plotted with statistical uncertainties in panel (a). The red solid, green dashed, blue dotted, and magenta dash-dotted histograms show the template mass spectra obtained from MC simulations of the η, $\pi^0\pi^0$, $\eta\pi^0$, and ω photoproduction processes, respectively. The thick black solid line shows a sum of all the template spectra. The plot in panel (b) shows the missing mass spectrum of a $\gamma\gamma$ pair in the real data. The line colors and styles of fit results are defined in the same way as those in (a).

IV. MEASUREMENT OF DIFFERENTIAL CROSS SECTIONS AND PHOTON BEAM ASYMMETRIES

A. Differential cross section

The differential cross sections were measured in 20 energy bins at $W = 1.82$–2.32 GeV and 16 polar angle bins at $\cos\theta^{\eta}_{\mathrm{c.m.}} = -1.0$–$0.60$. The differential cross section $d\sigma/d\Omega$ was calculated using the following equation:

$$\frac{d\sigma}{d\Omega} = \frac{Y_\eta}{N_\gamma\, T_\gamma\, F_{\mathrm{trans}}\, \rho_N\, A\, \mathrm{Br}_\eta\, \epsilon}\frac{1}{\Delta\Omega}. \qquad (1)$$

Y_η is the η photoproduction yield in a certain kinematic bin used for the cross section measurement. This value was obtained by counting the number of events after the requirement of signal selection conditions and subtracting backgrounds, as described in Secs. III B and III C. N_γ is the number of beam photons after correction by the dead time, described in Sec. III A. T_γ and F_{trans} are the photon-beam transmission rate and the energy-dependent correction factor, respectively, as described in Sec. III A. ρ_N is the number density of protons in the liquid hydrogen target (0.0708 g/cm^3). A is the geometrical acceptance of the detector system for each energy and angular bin, described in Sec. III D. Br_η is the branching fraction of the $\eta \to \gamma\gamma$ (0.3941). ϵ is the product of other efficiency factors, namely, the tagger reconstruction efficiency, the fraction of true tagger tracks after removing shower contributions, and the proton detection efficiency at the IPS or the DC. All of these efficiency factors are described in Sec. III A.

Systematic uncertainties for the measurement of differential cross sections are listed in Table I. The uncertainties due to the template fitting method are described in Sec. III C. The ambiguities for the energy-dependent transmission and the target length are the same as those described in Ref. [15]. The influence of the transverse shift of the photon beam is also reported in Ref. [15]. The amount of the shift should be consistent with that in Ref. [15], but the effect on the geometrical acceptance depends on the angular distribution of each reaction. So possible changes of the geometrical acceptance factors were reevaluated in individual kinematic bins by the MC simulation. The estimated variations of the cross section values were in the range of 0.01–8.8% depending on the kinematic bin. In the present analysis, the 99% confidence level cut was applied to select signals after the kinematic fit. For estimating the uncertainty due to the cut point, the differential cross section was recalculated by requiring the χ^2 probability to be greater than 5% so as to select a flat region in the probability distribution. The resulting changes were in

TABLE I. Systematic uncertainties of the differential cross section measurement

Source of systematic uncertainty	Typical value
Template fitting	
Fitting excl. the ω contribution	0.1–2.4%
Fitting with invariant mass	0.8–5.9%
Energy dependent transmission	
Fit function dependence	0.2–1.0%
Normalization method	2.8%
Energy dependence	0.3–2.0%
Target length	1.3%
Beam position shift	0.01–8.8%
Kinematic-fit cut dependence	0.01–3.4%
Tagger reconstruction efficiency	0.57–0.92%
Shower contribution	1.4%
Proton detection efficiency	0.09% (IPS) 0.45% (DC)
Branching ratio ($\eta \to \gamma\gamma$)	0.50%

TABLE II. Systematic uncertainties of the photon beam asymmetry measurement

Source of systematic uncertainties	Typical value
Uncertainty of the template fitting method	0.001–0.03
Difference of two polarization data	0.003–0.05
Another binning of azimuthal angle	0.004–0.05
Ambiguity of polarization vector direction	0.001–0.008
Uncertainty of laser polarization degree	0.04% of $\lvert\Sigma\rvert$

the range of 0.01–3.4%. Other systematic uncertainties come from the measurement of the tagger reconstruction efficiency, the shower contribution, and the proton detection efficiency, which are described in Sec. III A. The uncertainty of the branching fraction of the $\eta \to \gamma\gamma$ decay was also taken into account based on the Particle Data Group value [1]. The total systematic uncertainties were evaluated to be 3.4–13% by summing in quadrature the listed uncertainties.

B. Photon beam asymmetry

In the pseudoscalar-meson photoproduction with a linearly polarized beam, the differential cross section has an asymmetry depending on the azimuthal angle of the produced meson relative to the beam polarization direction. This is called photon beam asymmetry Σ. The Σ is defined in the center-of-mass system as

$$\frac{d\sigma}{d\Omega} = \frac{d\sigma_0}{d\Omega}[1 - P_\gamma \Sigma \cos(2\Phi)], \qquad (2)$$

where $\frac{d\sigma_0}{d\Omega}$ is the *unpolarized* differential cross section, P_γ is the degree of linear polarization of the photon beam, and Φ is the azimuthal angle between the linear polarization direction of the photon beam and the reaction plane of the η photoproduction. P_γ is calculated as a function of the photon beam energy based on the quantum electrodynamics [18]. The photon beam asymmetry Σ was determined by a fit to the yield distribution depending on the azimuthal angle Φ:

$$f(\Phi) = A[1 + B\cos(2\Phi)]. \qquad (3)$$

The fitting parameter B in Eq. (3) means the product of the photon beam polarization P_γ and the photon beam asymmetry Σ. Horizontally and vertically polarized photon beams were alternately used to reduce the systematic uncertainty arising from the incomplete detector symmetry. The angles of these polarization vectors were estimated to be -2.1° and 82.6° from the horizontal plane in the laboratory frame, respectively. The degree of laser polarization was typically 98%. P_γ was in the range of 42–91%, where the highest polarization was obtained at the Compton edge. The photon beam asymmetry was measured in ten energy bins at $W = 1.82$–2.32 GeV and eight polar angle bins at $\cos\theta^\eta_{\text{c.m.}} = -1.0$–$0.6$. At each kinematic bin, the sample was divided into 8 azimuthal-angle bins relative to the linear polarization vector of the photon beam.

Systematic uncertainties for the measurement of the photon beam asymmetries are listed in Table II. The listed numbers represent possible deviations in the Σ values, and the estimated deviations are distributed in the indicated range depending on the kinematic bin. For the measurement of the following uncertainties, neighboring kinematic bins were combined to reduce the influence of statistical uncertainty. First, the uncertainties of yield estimations by the template fitting method were evaluated in the same way as for the differential cross sections. Second, the difference between the photon beam asymmetries in the horizontal and vertical polarization data was examined to conservatively treat it as a possible systematic uncertainty. Third, the uncertainty due to different binning methods for azimuthal angles was estimated by shifting a half bin in the determination of bin ranges. Finally, the ambiguities of polarization vector direction and laser polarization degree were taken into account to estimate their influence on the photon beam asymmetries. The total systematic uncertainties were evaluated to be 0.008–0.09 by summing in quadrature the above uncertainties.

V. RESULTS

A. Differential cross section

The differential cross sections for the reaction $\gamma p \to \eta p$ were measured with the steps of 25 MeV and 0.1 in W and $\cos\theta^\eta_{\text{c.m}}$, respectively. Energy dependence of the measured differential cross sections is shown for individual $\cos\theta^\eta_{\text{c.m}}$ bins in Fig. 6 (red solid circles). The error bars are statistical uncertainties, and the gray histograms indicate the systematic uncertainties described in Sec. IV A. Also shown are the results of earlier works: LEPS [4] (black inverted triangles), CBELSA/TAPS [6] (green triangles), CLAS [5] (blue squares), and MAMI A2 [7] (black circles) experiments. The LEPS and CBELSA/TAPS results were obtained for the photon beam energy bins of 100 and 50 MeV, respectively. The CLAS results were obtained for the total energy bins of 10 MeV at $W = 1.68$–2.1 GeV and 5 MeV at $W = 2.1$–2.36 GeV. The MAMI A2 results were shown in fine energy bins of 2 to 10 MeV from threshold up to $W = 1.96$ GeV. All of those results were consistently binned with 0.1 steps in $\cos\theta^\eta_{\text{c.m}}$.

The present analysis has achieved precise and wide angular measurement by detecting all the final states, including a proton and an η meson which decays into $\gamma\gamma$. Although the proton momentum was treated as an unmeasured variable in the kinematic fit to obtain the results in Fig. 6, the validity of the procedure was confirmed by an independent cross-section measurement using the RPC, as discussed later. In contrast, the LEPS experiment detected only a proton emitted in the forward direction, and identified an η meson by a missing mass technique from the measured proton momentum in the limited acceptance $\cos\theta^\eta_{\text{c.m}} < -0.6$. The CLAS experiment provided esults of the highest statistical precision in a wide angular range, whereas the acceptance at backward η angles was limited to $\cos\theta^\eta_{\text{c.m}} > -0.855$. In addition, its experimental setup was optimized for the detection of charged particles, so the identification of the η meson was done using the $\eta \to \pi^+\pi^-\pi^0$ decay mode, where the π^0 was treated as a missing particle in the kinematic fit. The CBELSA/TAPS experiment analyzed η decays in the two modes $\eta \to \gamma\gamma$ and $\eta \to 3\pi^0 \to 6\gamma$ by using large acceptance calorimeters, which covered a wide angular region including the missing

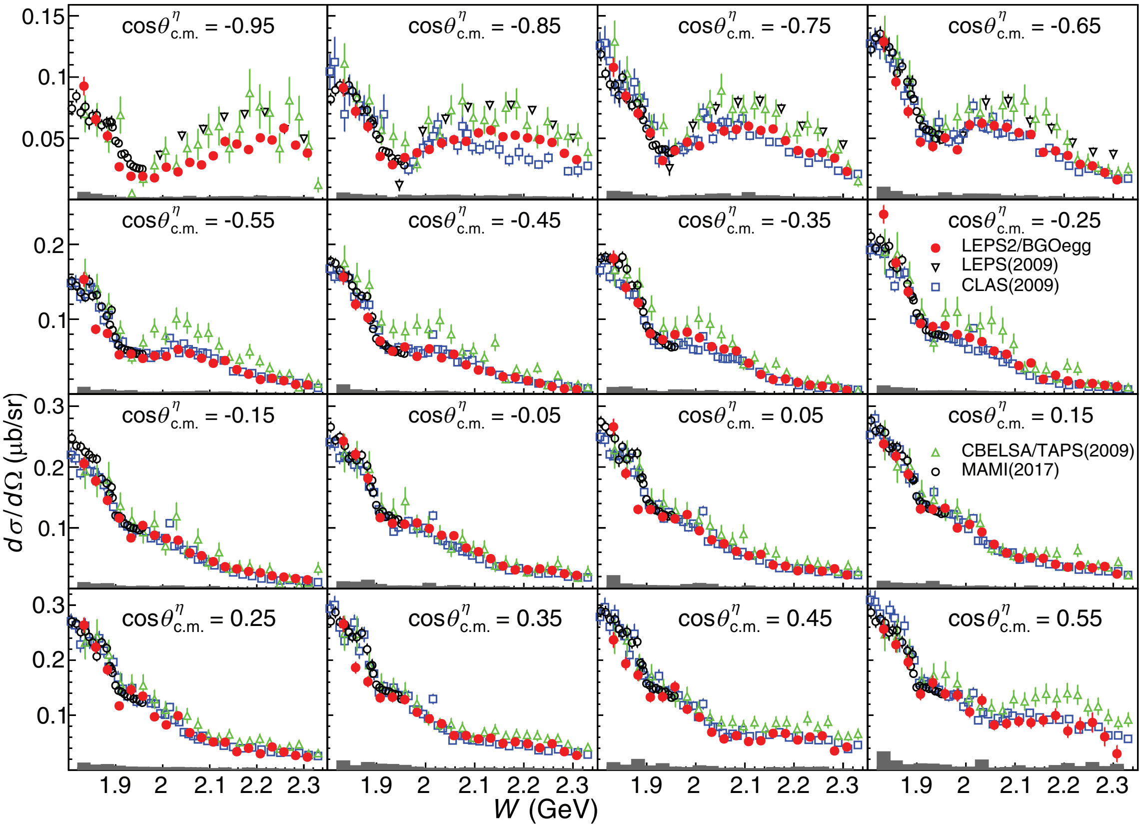

FIG. 6. Differential cross sections $d\sigma/d\Omega$ as a function of W for the reaction $\gamma p \rightarrow \eta p$. The individual panels correspond to different bins of the η emission angle in the center-of-mass system. The present results are shown by red solid circles with statistical uncertainties. The gray histograms are the associated systematic uncertainties. The green triangles, blue squares, black inverted triangles, and black circles come from other experimental results by the CBELSA/TAPS [6], CLAS [5], LEPS [4], and MAMI A2 [7] Collaborations, respectively.

backward η angles of the CLAS experiment. However, the statistics was limited compared with other experiments. The A2 Collaboration at MAMI measured η photoproduction with high statistics, but the covered energy range was lower than those of the other measurements.

The present results generally show a declining trend of differential cross sections as the energy increases in the region of $\cos\theta^{\eta}_{\mathrm{c.m.}} > 0$. A bump structure at higher energies appears in the region of $\cos\theta^{\eta}_{\mathrm{c.m.}} < 0$, and its strength becomes larger as the η emission angles get more backward. This bump position is around $W = 1.97$ GeV at $-0.1 < \cos\theta^{\eta}_{\mathrm{c.m.}} < 0$ and slightly shifts to $W = 2.02$ GeV at $-0.7 < \cos\theta^{\eta}_{\mathrm{c.m.}} < -0.6$. The peak position changes more rapidly at the most backward angles, and is around $W = 2.25$ GeV at $-1 < \cos\theta^{\eta}_{\mathrm{c.m.}} < -0.9$.

In $W < 2$ GeV, the differential cross sections obtained by the BGOegg, CLAS, CBELSA/TAPS, and MAMI A2 experiments are in agreement with each other at all the angular bins. At the higher energies, the BGOegg results agree with the CLAS data for $\cos\theta^{\eta}_{\mathrm{c.m.}} > -0.8$ while the CBELSA/TAPS and LEPS data inconsistently give larger cross sections compared to the other results. At backward η angles, the bump structure is seen in all the experiments but with different shapes and strengths. For instance, there is a discrepancy in the bump shape between the BGOegg and CLAS data at $-0.9 < \cos\theta^{\eta}_{\mathrm{c.m.}} < -0.8$, which corresponds to the acceptance boundary of the CLAS measurement. The amplitude of the bump in the LEPS measurement is significantly higher than the BGOegg result, although the peak positions of the two data sets agree with each other at the η angles $-0.9 < \cos\theta^{\eta}_{\mathrm{c.m.}} < -0.6$. At extremely backward angles $-1.0 < \cos\theta^{\eta}_{\mathrm{c.m.}} < -0.9$, both the peak position and strength of the bump are inconsistent between the BGOegg and LEPS results. The CBELSA/TAPS data at the corresponding η angles also show the bump structure but have large uncertainties, which make it difficult to examine the strength and shape of the observed structure in detail.

Because there are discrepancies in the differential cross section results among the different experiments at the extremely backward η angles, it is important to confirm the present measurement in a more precise manner. In order to provide reliability to the present results, an independent analysis of the same data set was additionally performed by detecting a proton at the RPC. The RPC can measure the momentum of a forward proton via its time of flight at the extremely backward η angles $(-1.0 < \cos\theta^{\eta}_{\mathrm{c.m.}} < -0.95)$. It thus provides the kinematically complete four-momentum conservation to be used in the kinematic fit without unmeasured variables. Figure 7 shows the comparison of differential cross sections obtained by using the RPC (green squares) and the same procedure as done for Fig. 6, only with the DC (red circles) in the overlapping acceptance region. These two analysis results are in good agreement both in the energy

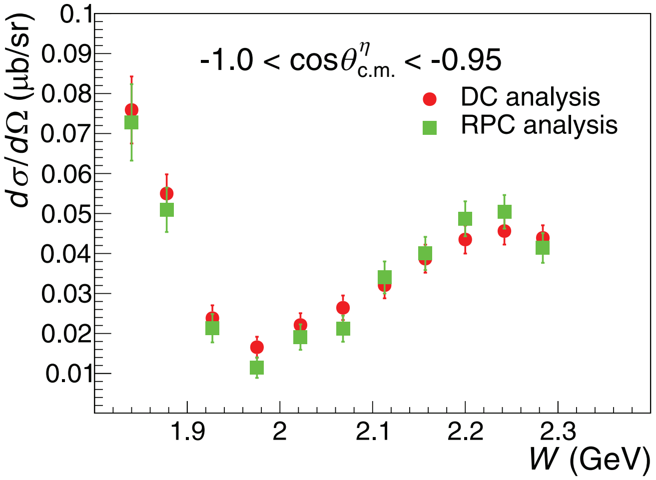

FIG. 7. Comparison of the differential cross sections with and without the use of RPC for the extremely backward η angles $-1.0 < \cos\theta^{\eta}_{\mathrm{c.m.}} < -0.95$. The red solid circles and green squares are the results by using the DC only and both the RPC and DC, respectively.

dependence and overall magnitude of the differential cross sections.

The angular distributions of differential cross sections for different energy bins are shown in Fig. 8. The present results (red points) show a backward rise in the higher energy region. The experimental results are compared with the PWA calculations by EtaMAID2018 [19,20] (blue solid lines), SAID2009 [21] (magenta dotted lines), Bonn-Gatchina2019 [22,23] (green dashed lines), and ANL-Osaka2016 [24,25] (black dotted-dashed lines). The EtaMAID2018 prediction agrees with the present data at total energies below 2.2 GeV, but not in the higher energy region, especially at the most backward angles. The SAID2009 calculations overestimate differential cross sections in the region of $W = 1.9$–2.0 GeV, and this disagreement disappears at the higher energies. However, the peaking structure of the SAID2009 calculation at $\cos\theta^{\eta}_{\mathrm{c.m.}} < -0.6$ and $W > 2.2$ GeV is not observed in the present data. The Bonn-Gatchina2019 calculations are more or less in agreement with the present data, reproducing the enhancement of differential cross sections at the backward angles. This is because their PWA fit utilizes all the data that are recently available prior to the present results. In the next subsection, the validity of the Bonn-Gatchina2019 model can be examined by the photon beam asymmetries that have been newly measured in the present analysis.

B. Photon beam asymmetry

The photon beam asymmetries for the reaction $\gamma p \to \eta p$ were measured with 50-MeV and 0.2 steps in W and $\cos\theta^{\eta}_{\mathrm{c.m.}}$,

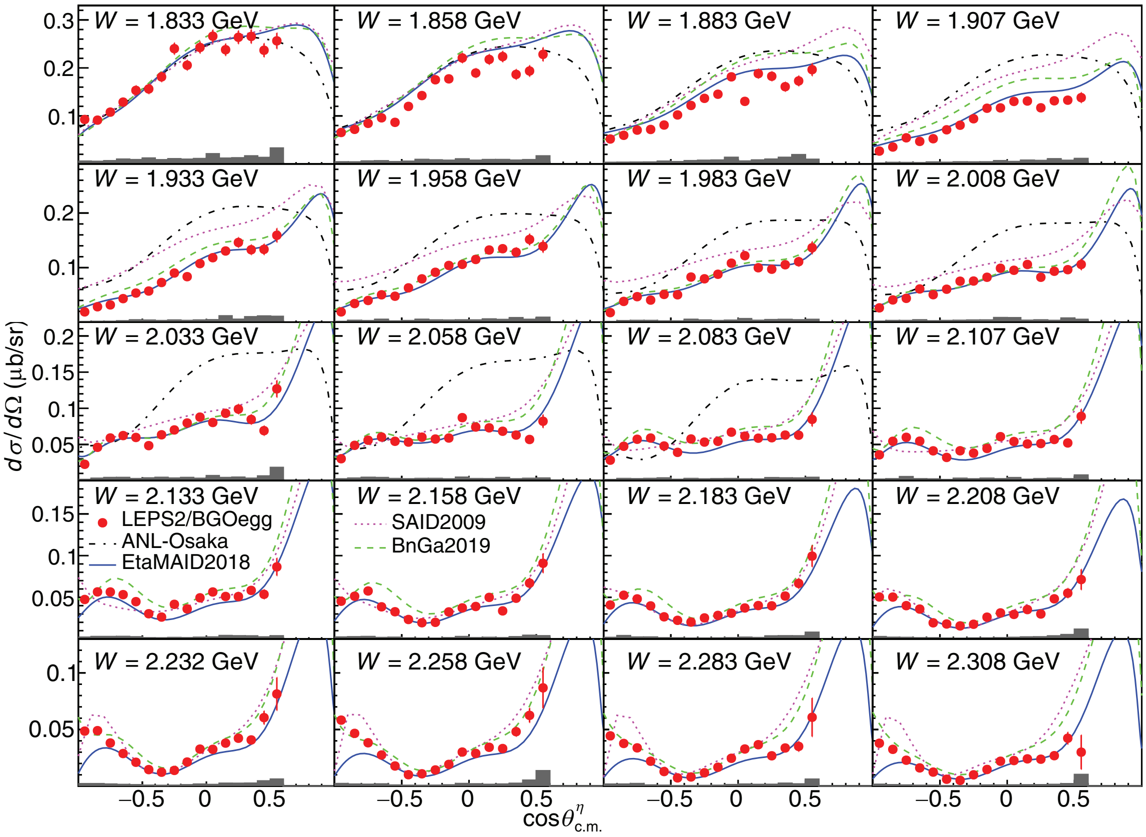

FIG. 8. Differential cross sections $d\sigma/d\Omega$ as a function of $\cos\theta^{\eta}_{\mathrm{c.m.}}$ for the reaction $\gamma p \to \eta p$. The present results are shown by red solid circles with statistical uncertainties. Estimated systematic uncertainties are indicated by the gray histograms. The blue solid, magenta dotted, green dashed, and black dash-dotted curves show the PWA model calculations by EtaMAID2018 [19], SAID2009 [21], Bonn-Gatchina2019 [22], and ANL-Osaka2016 [24], respectively.

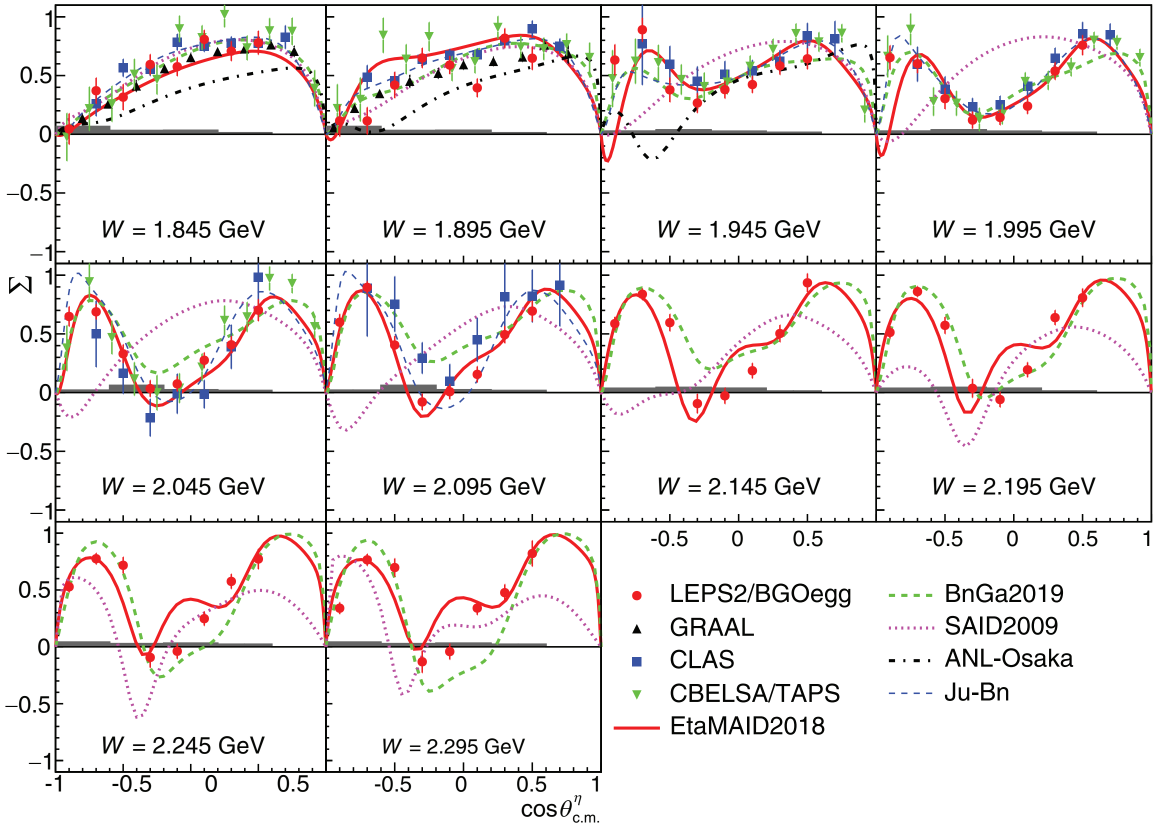

FIG. 9. Photon beam asymmetries Σ as a function of $\cos\theta^{\eta}_{\mathrm{c.m.}}$ for the reaction $\gamma p \to \eta p$. The present results are shown by the red solid circles with statistical uncertainties and the associated systematic uncertainties are shown by the gray histograms. The black triangles, blue squares, and green inverted triangles come from other experimental results by GRAAL [26], CLAS [8], and CBELSA/TAPS [9] Collaborations, respectively. The blue solid, green dashed, magenta dotted, black dash-dotted, and blue long-dashed curves represent the PWA results by the EtaMAID2018 [19], Bonn-Gatchina2019 [22], SAID2009 [21], ANL-Osaka [24], and Jülich-Bonn [27] models, respectively.

respectively. In the present work, precise Σ values in a wide angular range were obtained for the first time at the total energies above 2.1 GeV. Figure 9 show the measured photon beam asymmetries Σ with statistical uncertainties as a function of $\cos\theta^{\eta}_{\mathrm{c.m.}}$ (red solid circles). The gray histograms are the systematic uncertainties estimated in Sec. IV B. Each data point is plotted at the mean $\cos\theta^{\eta}_{\mathrm{c.m.}}$ value of entries in the corresponding angular bin. In Fig. 9, experimental results from the GRAAL [26], CLAS [8], and CBELSA/TAPS [9] Collaborations are also compared with the present results by the BGOegg experiment. Here all the overlaid results have used different energy-binning methods. The GRAAL results are divided into 15 photon beam energy bins in the E_γ range of 0.7–1.5 GeV, while the CBELSA/TAPS results have been obtained for the photon beam energy bins of each 60 MeV in the range of $E_\gamma = 1.13$–1.79 GeV. The CLAS experiment has adopted the photon beam energy bins of 27 and 40 MeV at $1.071 < E_\gamma < 1.689$ and $1.689 < E_\gamma < 1.876$ GeV, respectively. In Fig. 9, these results are plotted at the energies that are closest to the energy bins of the individual analyses.

The present results statistically agree with the other experimental results in the overlapping energy region below $W = 2.1$ GeV. The photon beam asymmetries have a dip structure around $\cos\theta^{\eta}_{\mathrm{c.m.}} = -0.2$ at $W > 1.9$ GeV. It has been suggested that this behavior is influenced by the helicity couplings for $N(1720)3/2^+$ and $N(1900)3/2^+$ [8]. The dip structure remains at higher energies, where new data are available by the present analysis.

The overlaid curves in Fig. 9 show the existing PWA results calculated by the EtaMAID2018 [19], Bonn-Gatchina2019 [22], SAID2009 [21], ANL-Osaka [24], and Jülich-Bonn [27] models. The ANL-Osaka and Jülich-Bonn results are limited to the total energy ranges below 1.95 and 2.1 GeV, respectively. The ANL-Osaka curve does not reproduce the experimental data in all energy regions because it does not include heavy-meson contributions such as an ω meson in the coupled-channel calculation. The SAID2009 curve does not reproduce the dip structure above $W = 1.95$ GeV. The EtaMAID2018, Bonn-Gatchina2019, and Jülich-Bonn models agree with the present results in the total energy region below 2.0 GeV except for the extremely backward region. In the region above 2.0 GeV, no PWA results reproduce the BGOegg results.

VI. DISCUSSION

A. Differential cross section enhancement at W = 2.0–2.3 GeV

In Fig. 8, the angular dependence of the differential cross section above $W = 2.1$ GeV shows an enhancement at

$\cos\theta^{\eta}_{\text{c.m.}} < -0.4$, where one can expect possible contributions from a u-channel exchange or high-spin s-channel resonances. Regge theory [28,29] allows us to assume a simple description of the smooth energy dependence for the u-channel cross section in the form of $s^{2\alpha(u)-2}$, where s and $\alpha(u)$ denote the center-of-mass energy and a Regge trajectory function, respectively. Therefore the bumplike energy dependence in a narrow range of $2.0 < W < 2.4$ GeV, as shown in Fig. 6, cannot be explained only by a u-channel contribution. The value of $2\alpha(u) - 2$ is expected to be negative in a small $|u|$ region, as shown in Fig. 33 of Ref. [30]. In addition, the EtaMAID2018 calculation describes the non-resonant background as s- and u-channel Born terms and t-channel vector meson exchanges. This calculation hints that the amplitude of the u-channel contribution is rather small [19]. The present data suggest that the steep backward rise of differential cross sections is likely related to the decay of high-spin s-channel resonances. In the photon-proton reaction, the helicity of the initial state is limited to $|h| \leqslant 3/2$. Therefore, if an intermediate resonance has a high spin ($J \geqslant 5/2$), it can emit an η meson to the backward or forward polar angles in two-body decays, as understood by the discussion of helicity amplitudes with Wigner d matrices [31]. The differential cross sections in the backward η angles are more sensitive to the high-spin s-channel resonances because of the suppression of t-channel meson exchanges.

Figure 10 shows the energy dependence of differential cross sections at $\cos\theta_{\text{c.m.}} = -0.95$, -0.85, -0.75, and -0.65 for the η, π^0, and ω photoproduction processes measured by the LEPS2/BGOegg C1ollaboration. The differential cross sections of π^0 and ω photoproduction were obtained using the same data set as the present analysis and reported in Refs. [15] and [32], respectively. The differential cross section distributions of the π^0 photoproduction show declining behaviors from 1.8 to 2.1 GeV. At the angle $\cos\theta^{\pi^0}_{\text{c.m.}} = -0.95$, a small enhancement above 2.1 GeV is seen, but there is no visible bump structure. The differential cross sections of the ω photoproduction also show no structures above 1.9 GeV. In contrast, only the η photoproduction shows a clear bump structure at the total energies above 2.0 GeV. In the flavor SU(3) quark models, the η meson contains $s\bar{s}$ quark pair in its composition while the π^0 and ω mesons have flavor configurations only with $u\bar{u}$ and $d\bar{d}$ quarks. Therefore, the observed bump structure in the differential cross sections of η photoproduction is likely associated with the nucleon resonances that have a large $s\bar{s}$ component and strongly couple to the ηN channel.

The position of the bump structure shifts from $W = 2.02$ GeV at $\cos\theta^{\eta}_{\text{c.m.}} = -0.65$ to $W = 2.25$ GeV at $\cos\theta^{\eta}_{\text{c.m.}} = -0.95$, as mentioned in Sec. V A. This may be caused by the presence of multiple resonances with isospin 1/2. In the mass range of 2.1–2.3 GeV, several resonances with three or four stars are currently known based on the πN-decay channel [e.g., $N(2100)1/2^+$, $N(2120)3/2^-$, $N(2190)7/2^-$, $N(2220)9/2^+$, $N(2250)9/2^-$] [1]. However, the information about the ηN decay of nucleon resonances is limited. The new BGOegg data of differential cross sections as well as photon beam asymmetries have high statistics at backward angles and provide additional constraints for the resonance search, particularly related to the bump structure.

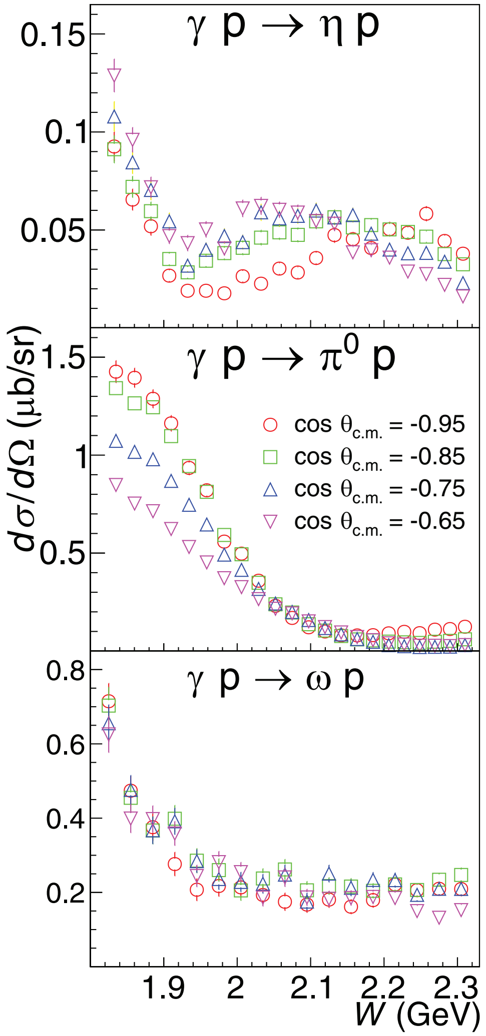

FIG. 10. The differential cross sections of the η, π^0, and ω photoproduction processes as a function of the total energy W at the angles $\cos\theta_{\text{c.m.}} = -0.95$ (red circles), -0.85 (green squares), -0.75 (blue triangles), -0.65 (magenta inverted triangles).

B. Comparison with the existing PWA results

The differential cross sections and photon beam asymmetries measured in the present analysis are in fair agreement with the existing PWA results at lower energies. In contrast, the PWA results at higher energies show clear differences from the present data, as described in Sec. V. The discrepancies in the photon beam asymmetries are particularly large. In addition, the PWA results are inconsistent with each other at the higher energies.

These discrepancies are clearly seen in Fig. 11, which compares the present data with existing PWA results calculated by the EtaMAID2018 [(a) and (b)] and Bonn-Gatchina2019 [(c) and (d)] models at the highest energy bin near $W = 2.3$ GeV. Here, differential cross sections and photon beam asymmetries are plotted in the left [(a) and (c)] and right [(b) and (d)] sides, respectively. For drawing the PWA curves of EtaMAID2018 and Bonn-Gatchina2019, the electromagnetic amplitudes, containing the information about the partial

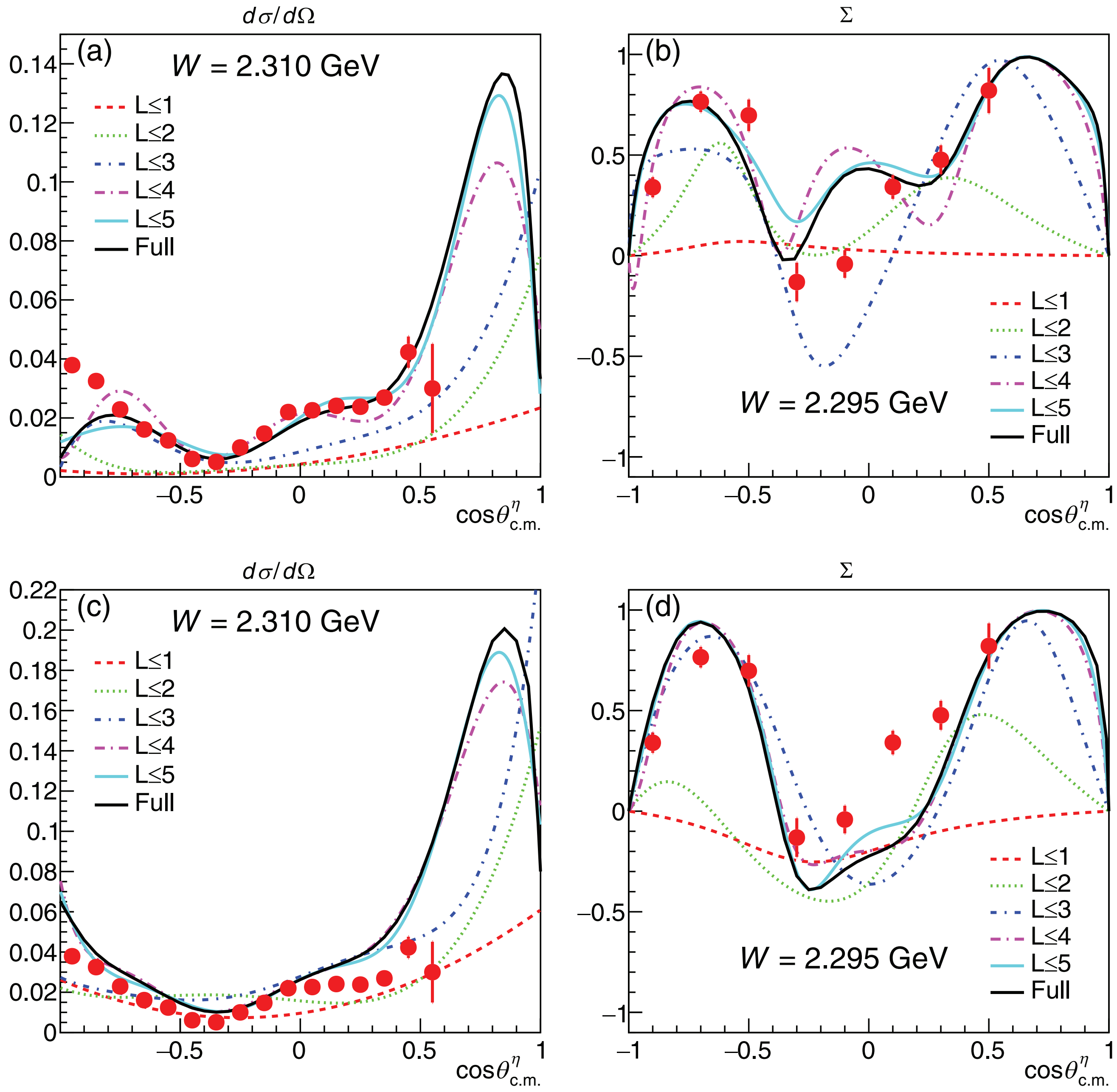

FIG. 11. The existing PWA results calculated by EtaMAID2018 [(a) and (b)] and Bonn-Gatchina2019 [(c) and (d)] with the orbital angular momenta L up to 1 (red dashed lines), 2 (green dotted lines), 3 (blue dotted-dashed lines), 4 (magenta long dashed-dotted lines), and 5 (cyan dotted lines). The full PWA calculation with all the orbital angular momenta is shown by black solid lines. The BGOegg results are plotted as red circles.

waves, were obtained from Refs. [20] and [23], respectively. The multipole amplitudes were combined with the Legendre polynomials to construct the Chew-Goldberger-Low-Nambu (CGLN) amplitudes [33], which are conventionally used for the pseudoscalar-meson photoproduction. In each panel, contributions from the partial waves up to the indicated orbital angular momenta (L) are also shown.

In Fig. 11 the EtaMAID2018 full calculation reproduces the measured differential cross sections except for the most backward η angles, where the experimentally observed backward rise does not exist in the calculated result. This calculation shows a small bump structure of photon beam asymmetry at $\cos\theta^{\eta}_{\rm c.m.} \approx 0$, while it is not seen in the experimental data. On the other hand, the Bonn-Gatchina2019 results reproduce the backward shape of differential cross sections but its strength is overestimated compared to the present results. The calculated photon beam asymmetry has no small bump structure like the EtaMAID2018 calculation but it is underestimated compared with the experimental data around $\cos\theta^{\eta}_{\rm c.m.} \sim 0$. Neither of these PWA models can reproduce the differential cross sections and the photon beam asymmetries simultaneously.

The different behaviors of backward cross sections in the two PWA results arise from the ambiguity of multipole contributions even at $L \leqslant 3$, as seen in Fig. 11. The different determinations of multipoles in the lower L region also cause a large difference between the calculated photon beam asymmetries especially at middle angles. It is clear that the current understanding of resonance and Born-term contributions is not enough even for lower L's at high energies. In addition, higher L contributions are important to reproduce the experimental data accurately.

Recently the Jülich-Bonn model calculation was updated by a fit to the differential cross sections and photon beam asymmetries in the η photoproduction measured by the CLAS experiment [8]. In this measurement, the photon beam asymmetries were obtained at $1.70 < W < 2.10$ GeV and $-0.8 < \cos\theta^{\eta}_{\mathrm{c.m.}} < 0.8$. Before the fit was made, the $N(1900)3/2^+$ was found to be important in the analyses of $K\Lambda$ and $K\Sigma$ photoproduction by the Bonn-Gatchina group [34]. In order to confirm this resonance contribution, the CLAS Collaboration fitted two sets of possible solutions with and without a contribution from the $N(1900)3/2^+$ resonance by using the Jülich-Bonn model. The CLAS data indicated the weakness of the $N(1900)3/2^+$ contribution in the η photoproduction, but was not able to clarify its strength because the difference between the two fits to the photon beam asymmetries should appear at extremely backward η angles, which were out of the CLAS acceptance. In contrast, the present results of photon beam asymmetries cover the most backward angles, while they are consistent with the CLAS results in the overlapping angular region. A refit of the Jülich-Bonn model to present data must provide more accurate information about the strength of the $N(1900)$ contribution.

VII. SUMMARY

Differential cross sections and photon beam asymmetries for the reaction $\gamma p \to \eta p$ were measured by detecting $\eta \to \gamma\gamma$ decays. A photon beam is produced by backward Compton scattering in the energy range of 1.3–2.4 GeV at the SPring-8 LEPS2 beamline. This photon beam is linearly polarized, and the degree of polarization is more than 90% at the Compton edge. Two γ's in the final state were measured using the BGOegg calorimeter, which has a large acceptance and the world's best energy resolutions. The direction of a proton in the final state was measured using the BGOegg calorimeter or the DC. A signal sample was selected by a kinematic fit using the four-momenta of two γ's, the direction of a final-state proton, the tagged photon beam energy, and a vertex position. The background estimation was done by template fitting.

The differential cross sections and photon beam asymmetries were derived in the kinematic bins of total energies and η polar angles covering 1.82–2.32 GeV and $-1.0 \leqslant \cos\theta^{\eta}_{\mathrm{c.m.}} \leqslant 0.6$, respectively. The validity of the present cross section measurement was confirmed by an independent analysis using the RPC, which additionally measured the momentum of a forward proton. A bump structure appears at $W = 2.02$–2.25 GeV in the case of $\cos\theta^{\eta}_{\mathrm{c.m.}} < 0$, and its strength becomes larger as the η emission angles get more backward. The bump structure is seen in the LEPS, CBELSA/TAPS, and CLAS experiments, but their shapes and strengths are different among these experiments. The present new measurement of differential cross sections provides high-precision and reliable data in the backward angular region. The bump-like enhancement indicates the contribution of high-spin nucleon resonances that contain a large $s\bar{s}$ component. The peak position of the bump structure moves depending on the η emission angle, suggesting the contribution of multiple resonances. For the first time, the photon beam asymmetry of the η photoproduction above $W = 2.1$ GeV was measured. No PWA calculations can reproduce the present results in the higher energy region. In addition, the multipole amplitudes of different PWA models are currently inconsistent with each other even at low orbital angular momenta. The present new results will provide additional constraints for the understanding of baryon resonances via PWAs.

ACKNOWLEDGMENTS

The experiment was performed at the BL31LEP of SPring-8 with the approval of the Japan Synchrotron Radiation Institute (JASRI) as a contract beamline (Proposal No. BL31LEP/6101). The authors are grateful to the staff at Spring-8 for supporting the commissioning of the LEPS2 beamline and providing excellent experimental conditions during the data collection. We thank T. Sato, A. Sarantsev, V. Nikonov, K. Nikonov, and D. Rönchen for discussions on the partial wave analyses. We appreciate A. Hosaka for discussions about the amplitude calculations. This research was supported in part by Ministry of Education, Culture, Sports, Science and Technology of Japan (MEXT), Scientific Research on Innovative Areas Grants No. JP21105003 and No. JP24105711, Japan Society for the Promotion of Science (JSPS) Grant-in-Aid for Specially Promoted Research Grant No. JP19002003, Grant-in-Aid for Scientific Research (A) Grant No. JP24244022, Grant-in-Aid for Young Scientists (A) Grant No. JP16H06007, Grants-in-Aid for JSPS Fellows No. JP24608, and the Ministry of Science and Technology of Taiwan.

---

[1] P. A. Zyla *et al.*, Prog. Theor. Exp. Phys. **2020**, 083C01 (2020).
[2] S. Capstick and W. Roberts, Prog. Part. Nucl. Phys. **45**, S241 (2000).
[3] L. D. Roper, Phys. Rev. Lett. **12**, 340 (1964)
[4] M. Sumihama *et al.*, Phys. Rev. C **80**, 052201 (2009).
[5] M. Williams *et al.*, Phys. Rev. C **80**, 045213 (2009).
[6] V. Crede *et al.*, Phys. Rev. C **80**, 055202 (2009).
[7] V. L. Kashevarov *et al.*, Phys. Rev. Lett. **118**, 212001 (2017).
[8] P. Collins *et al.*, Phys. Lett. B **771**, 213 (2017).
[9] F. Afzal *et al.*, Phys. Rev. Lett. **125**, 152002 (2020).
[10] N. Muramatsu *et al.*, Nucl. Instrum. Methods Phys. Res., Sect. A **1033**, 166677 (2022).
[11] N. Muramatsu *et al.*, Nucl. Instrum. Methods Phys. Res., Sect. A **737**, 184 (2014).

[12] T. Ishikawa *et al.*, Nucl. Instrum. Methods Phys. Res., Sect. A **837**, 109 (2016).
[13] N. Tomida *et al.*, J. Instrum. **9**, C10008 (2014).
[14] N. Tomida *et al.*, J. Instrum. **11**, C11037 (2016).
[15] N. Muramatsu *et al.*, Phys. Rev. C **100**, 055202 (2019).
[16] http://www.spring8.or.jp/ja/users/operation_status/schedule/bunch_mode.
[17] S. Agostinelli *et al.*, Nucl. Instrum. Methods Phys. Res., Sect. A **506**, 250 (2003); J. Allison *et al.*, IEEE Trans. Nucl. Sci. **53**, 270 (2006).
[18] A. D'Angelo, O. Bartalini, V. Bellini, P. Levi Sandri, D. Moricciani, L. Nicoletti, and A. Zucchiatti, Nucl. Instrum. Methods Phys. Res., Sect. A **455**, 1 (2000).
[19] L. Tiator *et al.*, Eur. Phys. J. A **54**, 210 (2018).
[20] https://maid.kph.uni-mainz.de/eta2018/etamaid2018.html.
[21] http://gwdac.phys.gwu.edu/.
[22] J. Müller *et al.* (CBELSA/TAPS Collaboration), Phys. Lett. B **803**, 135323 (2020).
[23] https://pwa.hiskp.uni-bonn.de/.
[24] H. Kamano, S. X. Nakamura, T.-S. H. Lee, and T. Sato, Phys. Rev. C **94**, 015201 (2016).
[25] T. Sato (private communication).
[26] O. Bartalini *et al.*, Eur. Phys. J. A **33**, 169 (2007).
[27] D. Rönchen *et al.*, Eur. Phys. J. A **51**, 70 (2015).
[28] P. D. B. Collins, *An Introduction to Regge Theory and High Energy Physics* (Cambridge University Press, Cambridge, 1977).
[29] J. K. Storrow, Rep. Prog. Phys. **50**, 1229 (1987).
[30] J. M. Laget, Prog. Part. Nucl. Phys. **111**, 103737 (2020).
[31] C. G. Fasanoand, F. Tabakin, and B. Saghai, Phys. Rev. C **46**, 2430 (1992)
[32] N. Muramatsu *et al.*, Phys. Rev. C **102**, 025201 (2020).
[33] G. F. Chew, M. L. Goldberger, F. E. Low, and Y. Nambu, Phys. Rev. **106**, 1345 (1957).
[34] A. V. Anisovich, R. Beck, E. Klempt, V. A. Sarantsev, and U. Thoma, Eur. Phys. J. A **48**, 88 (2012).